RSC Advances

PAPER

View Article Online
View Journal | View Issue

Cite this: *RSC Adv.*, 2024, **14**, 35064

Improved energy storage performance and thermal stability of hafnium-substituted strontium sodium niobate tungsten bronze ceramics

Wenbin Feng, †* Lele Ding,† Jiajia Zhang, Chunyi Zhu and Shenzhenyi Song

Dielectric capacitors are widely used in the field of pulsed power systems owing to their ultra-fast charge and discharge capacity; however, considering the complex environment they face in practical applications, how to further improve their thermal stability is an urgent issue that needs to be solved. Tungsten bronzes have the potential to broaden the temperature stability range owing to their unique structure, but only few studies have focused on them. Herein, lead-free $Sr_{4-x}La_xNa_2Hf_xNb_{10-x}O_{30}$ ceramics with a tungsten bronze structure were synthesized, and their energy storage properties were comprehensively characterized. With proper Hf substitution in the B site and rare earth substitution in the A site, significantly enhanced relaxor behavior is induced, leading to a broad plateau of the dielectric curve, slim polarization–electric field loop, high energy storage efficiency and stable capacitive performance over a wide temperature range. In addition, an improved microstructure with fewer defects, decreased average grain size, increased band gap and resistance were obtained, which benefit to the increase in breakdown strength and energy storage density. Finally, improved energy storage performance and thermal stability were achieved for the compounds, with W_{total} = 3.6 J cm^{-3}, W_{rec} = 2.9 J cm^{-3}, η = 80% and stable temperature range = 20–160 °C. Thus, the current system is a promising candidate for application in temperature-stable dielectric capacitors.

Received 30th August 2024
Accepted 22nd October 2024

DOI: 10.1039/d4ra06275b

rsc.li/rsc-advances

1. Introduction

Dielectric capacitors have ultrahigh power density and ultrafast charging and discharging capabilities. Their charging and discharging processes can reach the level of microseconds or even nanoseconds, and they have the advantages of good thermal stability, long service life, and greater safety and reliability.[1–3] They are very suitable for fields requiring high power density such as mobile electronic devices as well as military and hybrid electric vehicles. However, compared with the energy storage density of electrochemical capacitors and batteries, that of dielectrics is very limited. With the development of power electronic devices and systems towards miniaturization, lightweight and integration, developing dielectric capacitors with high energy storage density is of great significance. Energy stored per unit volume of a dielectric material is defined as energy density (W), which can be expressed as follows:

$$W = \int_0^{D_{max}} E \mathrm{d}D,$$

where D is the electric displacement in the dielectric layer, D_{max} is the maximum electric displacement, and E is the electric field applied to the dielectric material.[4] For ferroelectrics, relaxor ferroelectrics and anti-ferroelectrics with high dielectric constant, D is approximately equal to polarization (P). Therefore, the above formula can be expressed as follows:

$$W = \int_0^{P_{max}} E \mathrm{d}P,$$

$$W_{rec} = \int_{P_r}^{P_{max}} E \mathrm{d}P.$$

Another important parameter for energy storage capacitors is energy efficiency (η), which is the ratio of recoverable energy density (W_{rec}) to the total energy density (W):

$$\eta = \frac{W_{rec}}{W} \times 100\%.$$

It can be seen from the above equations that high maximum polarization and breakdown strength are beneficial to improve the energy density of dielectric materials. In addition, low dielectric loss and remanent polarization contribute to higher energy efficiency of capacitors. At the same time, pulsed power

Jiangsu Key Laboratory of Zero-Carbon Energy Development and System Integration, School of Environmental Science, Nanjing Xiaozhuang University, Nanjing, 211171, China. E-mail: fwbnx@njxzc.edu.cn

† These authors contributed equally to this work.

devices are often faced with complex environments in practical applications. The temperature range of −50 °C to 200 °C or higher puts forward extremely high requirements for the temperature stability of dielectric capacitors. Therefore, how to further broaden the temperature stability range of dielectric capacitors is an important issue that needs to be solved urgently.

Compared with normal ferroelectric and anti-ferroelectrics, which have large polarization, the sensitivity of dielectric constant and polarization intensity to temperature for relaxor ferroelectric materials is reduced due to the unique nanopolar micro-region, which is beneficial to obtain stable properties in a wide temperature range.[5,6] Meanwhile, relaxor ferroelectric materials usually have large dielectric constant, saturation polarization, slender hysteresis loop and extremely low remanent polarization, this is quite helpful to obtain both large energy storage density and energy storage efficiency.[7–9] Furthermore, the barrier for dynamic domain switching in relaxor ferroelectrics is much lower, this will significantly improve the fatigue resistance and breakdown strength of these materials and contribute to the development of dielectric materials with outstanding overall energy storage capabilities.[2,10]

Tungsten bronze dielectric is the second largest family of dielectrics after perovskite, taking tetragonal tungsten bronze as an example, the unit cell of tetragonal tungsten bronze is composed of a lattice network formed by the common vertex connection of 10 oxygen octahedra BO_6. The voids between oxygen octahedra can be divided into three different types: quadrilateral A1 voids, pentagonal A2 voids and triangular C voids. The general structure is $A1_2A2_4C_4B1_2B2_8O_{30}$.[11] Its unique structure makes it feasible to manipulate the relaxor or normal ferroelectric behaviors by A and B site cation substitutions. $Sr_2NaNb_5O_{15}$ ceramic is an important tungsten bronze material characterized by its high dielectric permittivity, high saturation polarization, and low dielectric loss over a wide temperature range. Previous studies have identified two significant dielectric permittivity anomalies in $Sr_2NaNb_5O_{15}$. The one observed at high temperatures is associated with the transition from a paraelectric phase to a ferroelectric phase. Meanwhile, the second anomaly that occurs at lower temperatures is linked to low-temperature dielectric relaxation, which is frequently seen in various tungsten bronzes as a result of their distinctive local structural disorder.[12–14] These anomalies create a broad plateau of dielectric constant stability over a wide temperature range. Therefore, $Sr_2NaNb_5O_{15}$ shows promise for developing dielectric energy storage materials that maintain high thermal stability across a wide temperature spectrum. However, research on $Sr_2NaNb_5O_{15}$ remains relatively limited, suggesting a need for further exploration to fully harness its potential for energy storage applications.

According to previous studies, replacing the B-site ferroelectric active cation Nb^{5+} with non-ferroelectric active cations such as Ta^{5+} and Zr^{4+} in tungsten bronzes will disrupt the long-range polarization sequence of Nb–O–Nb–O bonds, promote the formation of polar nanomicroregions, and enhance the ferroelectric relaxation characteristic of the materials.[15–19] In addition, the substitution of Ta^{5+} and Fe^{3+} has a significant effect on grain refinement, which can inhibit the abnormal growth of grains and improve the microstructure. At the same time, the proper addition of these cations also increases the band gap of the material and improves the resistance and insulation.[16,19,20] Recent studies have shown that substituting Hf in tungsten bronze ceramics can also inhibit the abnormal growth of the grain size and increase the microstructure homogeneity.[21] This Hf substitution in the B site may also induce local charge and lattice disorder for the NbO_6 matrix, promoting the formation of polar nanoregions and leading to a relatively stronger relaxor nature. However, the impact of Hf substitution on the energy storage properties of tungsten bronzes has not been extensively explored and it is worthwhile to make a systematic investigation. Additionally, rare earth elements substituted at the A site have been reported to have the effect of enhancing the ferroelectric and energy storage properties,[22,23] therefore, in order to maintain electrical neutrality, La^{3+} is added to the matrix to substitute at the A site.

In this work, we prepared and synthesized lead-free $Sr_{4-x}La_xNa_2Hf_xNb_{10-x}O_{30}$ tungsten bronze structural ceramics, and systematically characterized their dielectric, ferroelectric and energy storage performances. Compared with $Sr_4Na_2Nb_{10}O_{30}$, the Hf substitution in the B site significantly enhances the relaxor ferroelectric behavior and improves the dielectric breakdown strength. As a result, a high total energy storage density of 3.6 J cm^{-3}, energy storage efficiency of 80%, and good thermal stability are achieved simultaneously in the compounds under an electric field of 360 kV cm^{-1}. The current system represents a promising candidate for use in temperature-stable dielectric capacitors.

2. Experimental details

$Sr_{4-x}La_xNa_2Hf_xNb_{10-x}O_{30}$ ($x = 0$, 0.2, 0.4 and 0.6) ceramics were prepared using the solid–state reaction method. The raw materials included $SrCO_3$ (99.95%), La_2O_3 (99.99%), Na_2CO_3 (99.99%), HfO_2 (98%), and Nb_2O_5 (99.9%). These were mixed in stoichiometric proportions and ball milled for 6 hours using zirconia balls and ethanol. The resulting mixtures were dried and calcined at 1250 °C for 3 hours. The powders were then re-milled and pressed into pellets with a diameter of 12 mm and a thickness of approximately 2 mm. The pellets were sintered at temperatures ranging from 1275 °C to 1325 °C for 3 hours to produce dense ceramics.

The crystalline structures of the prepared ceramics were identified using powder X-ray diffraction (XRD) patterns obtained with a diffractometer (SmartLab SE, Rigaku Co., Japan) utilizing Cu Kα radiation. After polishing and thermal etching at 1225 °C for 30 minutes, the samples' microstructures were examined using scanning electron microscopy (SEM) (Scios 2 Hivac, FEI, America). Raman spectra were measured using a Raman spectrometer (DXR, Thermo Scientific, America) with ceramic powders. The diffuse reflectance and transmittance spectra were obtained using a UV-vis-NIR spectrophotometer (UV-3600i Plus, Shimadzu, Japan) within the wavelength of 200–860 nm. The dielectric characteristics were evaluated using an

LCR analyzer (Agilent 4294A, Santa Clara, CA) with a temperature-controlled cavity (VDMS 2000, Partulab, China) over a temperature range of −100 °C to 350 °C and a frequency range of 100 Hz to 1 MHz. The silver paste was used as electrodes before measurement. The *P*–*E* hysteresis loop and energy storage properties were assessed using a Precision Materials Analyzer (RT Premier II, Radiant Technologies Inc., NM), with gold sputtered on both sides of the ceramics serving as the electrodes.

3. Results and discussion

Dense ceramic samples of $Sr_{4-x}La_xNa_2Hf_xNb_{10-x}O_{30}$ were successfully synthesized with measured densities of 4.78, 4.87, 4.96 and 4.98 g cm^{-3} for $x = 0$, 0.2, 0.4 and 0.6, and the corresponding relative densities are 94.0%, 94.3%, 95.1% and 94.2%, respectively. The crystal structure was characterized using X-ray diffraction (XRD) analysis and the patterns are shown in Fig. 1(a). According to PDF#34-0429, these samples exhibit a tetragonal tungsten bronze structure with no secondary phases detected. For $x = 0$, Sr^{2+} cations substitute the A2 site while Na^+ cations occupy the A1 site, with Nb^{5+} cations distributed across both B1 and B2 sites. For x = 0.2–0.6, Sr^{2+} and La^{3+} cations co-occupy the A2 site, Na^+ cations still substitute at the A1 site, while Hf^{4+} and Nb^{5+} cations are jointly located at B1 and B2 sites. As the substitution amount of Hf and La increases, the lattice spacing initially decreases and then increases, as can be seen in Fig. 1(b). This variation is attributed to the different cationic radii of Hf^{4+} (0.071 nm) compared to Nb^{5+} (0.064 nm), and La^{3+} (0.136 nm) compared to Sr^{2+} (0.144 nm). At $x < 0.4$, the smaller size of La^{3+} compared to Sr^{2+} primarily leads to the decrease in lattice spacing, whereas for $x > 0.4$, the effect of the larger size of Hf^{4+} substitution for Nb^{5+} becomes predominant, resulting in increased lattice spacing, the trend is the balance of the above two factors. It can be inferred that these substitutions may induce local compositional, charge, and lattice disorders, which may consequently impact the capacitive performance of the compounds.

To further explore the effect of cation substitution on the local structure, Raman spectroscopy measurement was performed under the same conditions for all samples and the results are shown in Fig. 2. The Raman vibration modes for tungsten bronzes include three distinctive internal modes (ν_1, ν_2, and ν_5), which originate from the vibrations of the BO_6 octahedra, as well as several external modes were typically observed at low wave numbers that are primarily associated with A site vibrations and symmetry changes.[24,25] The three internal Raman vibration modes appear around 250 cm^{-1}, 630 cm^{-1}, and 845 cm^{-1} for all compounds, corresponding to ν_1, ν_2, and ν_5, respectively. The bending and stretching of the BO_6 octahedra correspond to the modes at 250 cm^{-1} and 630 cm^{-1}, respectively, while the deformation of BO_6 is relevant to the mode at 845 cm^{-1}. As the x value increases, both the wavenumber and full width at half maximum (FWHM) for the Raman modes exhibited notable changes. The wavenumber for the ν_1 Raman mode remains stable, whereas ν_2 and ν_5 display a red shift with increasing x, as illustrated in Fig. 2(b). The bending mode ν_5 undergoes a gradual change with increasing x, while the stretching mode ν_2 shows an abrupt change at $x = 0.2$, and then remains relatively stable from $x = 0.2$ to $x = 0.6$. The red shift of these internal modes is linked to the expansion of the octahedra and a decrease in the strength of the B–O bonds, this is the indicator of stronger relaxation behavior and a diminished intensity of polarization.[26] The FWHM values

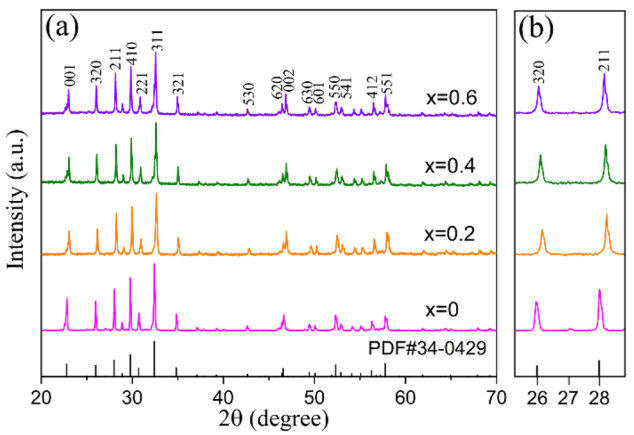

Fig. 1 (a) XRD patterns of $Sr_{4-x}La_xNa_2Hf_xNb_{10-x}O_{30}$ (x = 0, 0.2, 0.4 and 0.6) ceramics; (b) partial enlargement drawing of diffraction peaks of (320) and (211).

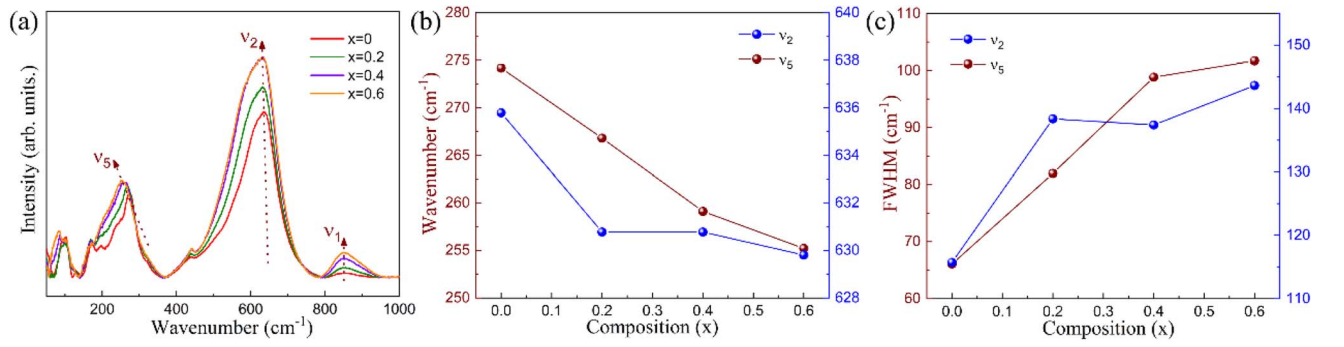

Fig. 2 (a) Raman spectra for $Sr_{4-x}La_xNa_2Hf_xNb_{10-x}O_{30}$ (x = 0, 0.2, 0.4 and 0.6) ceramics at ambient temperature; (b) Raman shift of the ν_2 and ν_5 modes; (c) full width at half maximum (FWHM) of the ν_2 and ν_5 modes.

(Fig. 2(c)) for ν_2 and ν_5 are larger for $x = 0.2$, 0.4 and 0.6 compared to $x = 0$ and remain stable at $x = 0.4$ and $x = 0.6$. Generally, the increased local structural disorder results in broader Raman modes and larger FWHM values.[24] Therefore, the observed Raman shifts and changes in FWHM values in the Raman data inevitably confirmed the stronger local structural disorder for this compound with increasing Hf substitution in the B site and La substitution in the A site, and this will undoubtedly affect the dielectric and ferroelectric characteristics.

The microstructures of all samples were analyzed and are presented in the scanning electron microscope (SEM) images, see Fig. 3(a)–(d). All samples display a pillar grain morphology, suggesting that the cell parameter c is less than a and b. Variations in cation substitution result in distinct changes in both grain size and defect density. As x increases from 0 to 0.6, the grain size distribution, shown in Fig. 3(e)–(h), reveals that the smallest grain size of 3.7 μm occurs at $x = 0.4$, which demonstrates a dense microstructure devoid of significant porosity, consistent with the observed high relative density for this compound. Previous studies have indicated that appropriate Hf substitution may promote the formation of finer grains and reduce defects, thereby enhancing dielectric breakdown strength and energy storage density. In this instance, proper Hf substitution also has the effect of producing a more dense and uniform structure. However, when x increases from 0.4 to 0.6, the sintering temperature rises from 1275 °C to 1325 °C, this higher sintering temperature for $x = 0.6$ will inevitably lead to the growth of the grain size,[27–29] so the observed microstructure is the consequence of the synergistic impact of Hf substitution induced grain refinement and the sintering temperature-induced grain size change on morphology. With x increasing to 0.6, the effect of higher sintering temperature plays a leading role and the grain size shows slight growth. The most uniform microstructure with the least defects and smallest grain size is observed for $x = 0.4$.

The dielectric breakdown strength E_b is closely associated with a uniform and dense microstructure, as well as a large band gap. To evaluate the band gap of all compounds, UV-vis absorption spectra were measured and are presented in Fig. 4. Theoretically, determining the band gap requires establishing the relationship between $(\alpha h\nu)^2$ and $h\nu$, where α represents the absorption coefficient. However, since α cannot be measured directly and is proportional to the absorbance A, using either A or α does not impact the calculated value of the band gap E_g, therefore, for simplicity, absorbance A can be utilized in place of α.[30] A larger band gap E_g typically indicates higher insulation properties and enhanced dielectric breakdown strength. It can be seen from Fig. 4(b) that among all the samples, $x = 0$ exhibits the smallest band gap of 3.33 eV. As x increases, the band gap first rises and then decreases, presenting values of 3.42 eV, 3.40 eV, and 3.37 eV for $x = 0.2$, 0.4, and 0.6, respectively. It can be inferred that the substitution of Hf significantly increases the band gap value and enhances insulation compared to $x = 0$, this is beneficial to improve the dielectric breakdown strength and energy storage performance. However, excessive Hf content may reduce the band gap again and diminish this effect, for example, when x increases to 0.6, the band gap decreases to 3.37 eV, because in this compound, La is also substituted in A site in order to balance the charge and induce stronger relaxor nature. Many reports focused on ferroelectric and energy storage ceramics have found that La substitution can slightly decrease the band gap,[31–33] therefore, considering the above factor, the changing trend of the band gap must be the combined effect of Hf and La substitutions.

In order to obtain more accurate results about the electrical properties of grain and the grain boundaries,[34,35] the high–temperature complex impedance spectra for all samples were measured at 400 °C, with the results presented in Fig. 5. All data points align well with an elliptical curve, suggesting that both grains and grain boundaries contribute to the electrical response, and some degree of electrical heterogeneity exists

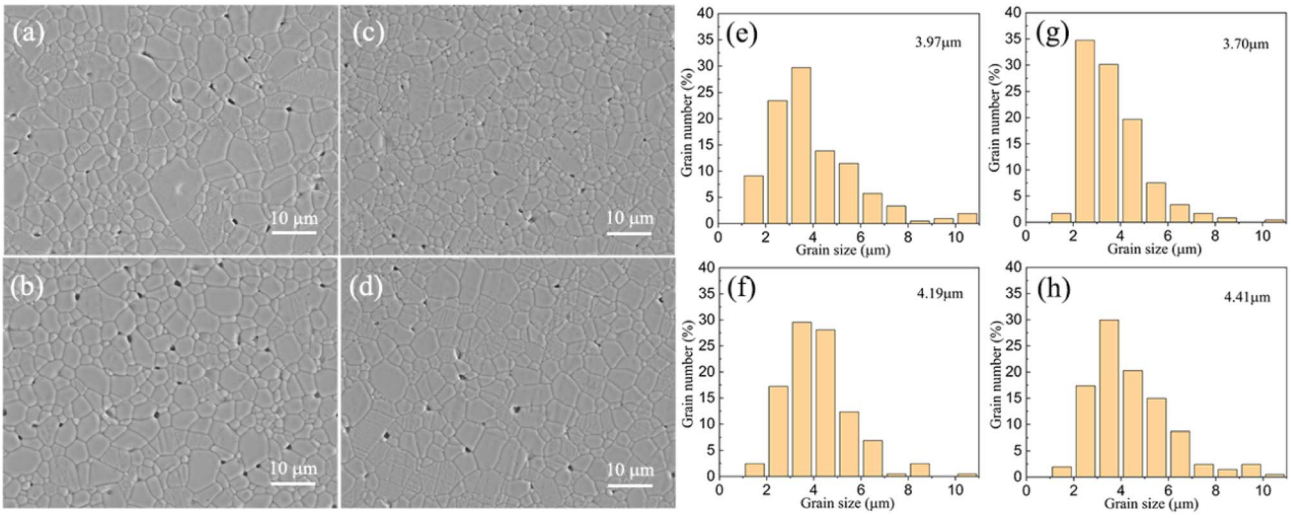

Fig. 3 SEM micrographs of the polished and thermally etched surfaces of $Sr_{4-x}La_xNa_2Hf_xNb_{10-x}O_{30}$ ceramics: (a) $x = 0$, (b) $x = 0.2$, (c) $x = 0.4$, (d) $x = 0.6$. The grain size distribution of the samples corresponding to (a–d): (e) $x = 0$, (f) $x = 0.2$, (g) $x = 0.4$, (h) $x = 0.6$.

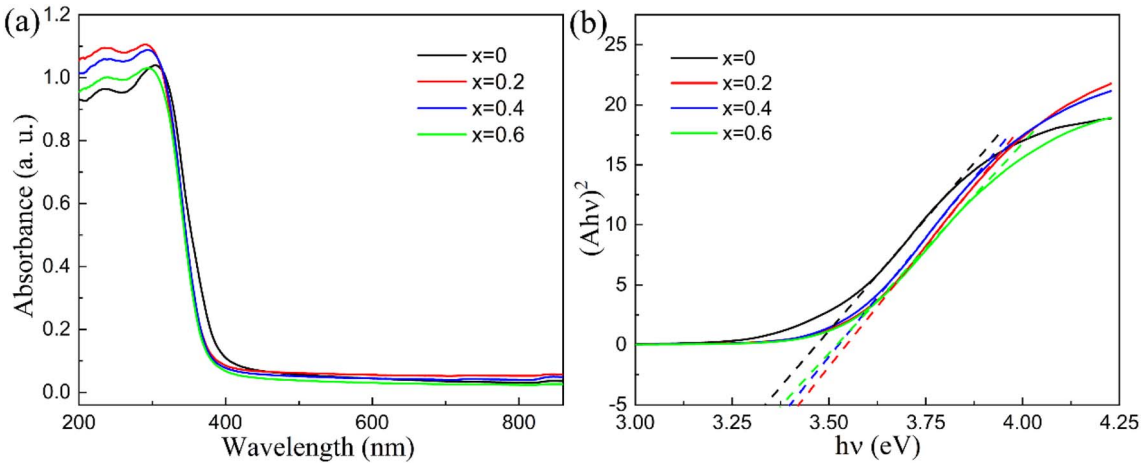

Fig. 4 (a) UV-vis absorption spectrum for $Sr_{4-x}La_xNa_2Hf_xNb_{10-x}O_{30}$ ($x = 0$, 0.2, 0.4 and 0.6); (b) $(Ahv)^2$ *vs.* hv plots for $Sr_{4-x}La_xNa_2Hf_xNb_{10-x}O_{30}$ ($x = 0$, 0.2, 0.4 and 0.6).

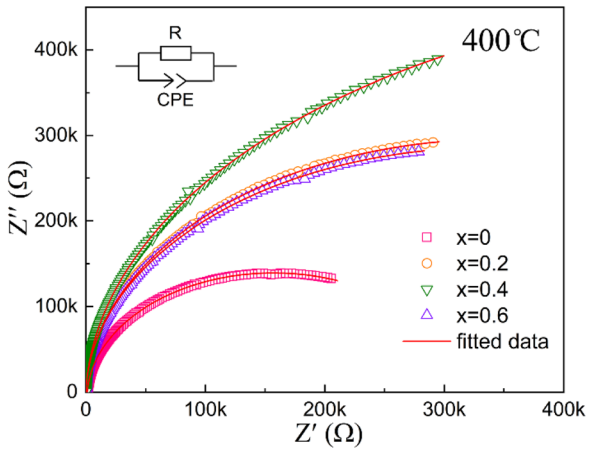

Fig. 5 Complex impedance spectrum at 400 °C for $Sr_{4-x}La_xNa_2Hf_xNb_{10-x}O_{30}$ ($x = 0$, 0.2, 0.4 and 0.6) ceramics. The red line indicates the fitted data. The inset shows the equivalent circuit diagram of the impedance data.

within the compounds. Apparently, Hf substitution increases the resistance of the compound. As the value of x increases, the resistance initially rises from $x = 0$ to $x = 0.4$, followed by a decrease from $x = 0.4$ to $x = 0.6$. This trend suggests that electrical heterogeneity is suppressed at $x = 0.4$. It has been reported that incorporating additional cations into the matrix can effectively reduce microstructural and electrical heterogeneity.[20,36,37] The development of a homogeneous electrical microstructure will make the occurrence of electrical breakdown more difficult, thereby enhancing dielectric breakdown strength E_b. The inclusion of Hf and La within the $Sr_4Na_2Nb_{10}O_{30}$ matrix contributes to improved electrical uniformity and increased resistance, which may create favorable conditions for enhancing both E_b and energy storage density in the material.

The temperature-dependent dielectric constant and dielectric loss curves are presented in Fig. 6(a)–(d). For $x = 0$, the peak at 330 °C corresponds to the transition from a paraelectric phase 4/*mmm* to a ferroelectric phase 4 mm, while the one between −29 °C and 0 °C is associated with the low-temperature dielectric relaxation commonly found in many tungsten bronzes due to their specific local structural disorder.[12,38,39] As x increases, the high-temperature dielectric anomaly shifts to the left, and eventually merges together with the low-temperature peak for $x = 0.4$ and $x = 0.6$. For $x = 0$, the temperature of the ferroelectric transition peak remains consistent at approximately 330 °C for different frequencies. However, as x increases, the dielectric peak shows a more diffused nature with stronger frequency dispersion in the dielectric constant curve. This suggests that Hf substitution strongly enhances the relaxor nature of the compound. Moreover, the dielectric constant value also decreases gradually with increasing x. Based on our previous studies of $Sr_4Na_2Nb_{10}O_{30}$ with the experimental result in this study, further increase of x will not lower the Curie point again but only lead to lower dielectric constant and ferroelectric polarization, and this is normally unfavorable to high energy storage performance, so x is only limited to 0.6. In general, tungsten bronzes containing Hf display less ferroelectric activity and exhibit a weaker displacement in the BO_6 octahedra along the polar axis. The substitution of Hf for Nb induces local variations in composition, charge, and lattice structure within the NbO_6 framework, which disrupts the long-range Nb–O–Nb–O polar order. This disruption can lead to the emergence of local random fields and promote the development of polar nano-regions. As a result, the introduction of Hf at the B site leads to the change of transition type from normal ferroelectric to relaxor ferroelectric. This change significantly lowers the temperature of the first dielectric anomaly from 330 °C to −20 °C, and even leads to the merging of the two dielectric anomalies at higher levels of Hf substitution. Meanwhile, alongside this enhanced relaxor nature, the thermal stability of the samples' dielectric properties improves significantly with increasing x. As illustrated in Fig. 6(e), using 0 °C as a standard, the thermal stability measured by permittivity variation was within 15% and the corresponding temperature ranges are: −62 °C to 75 °C for x

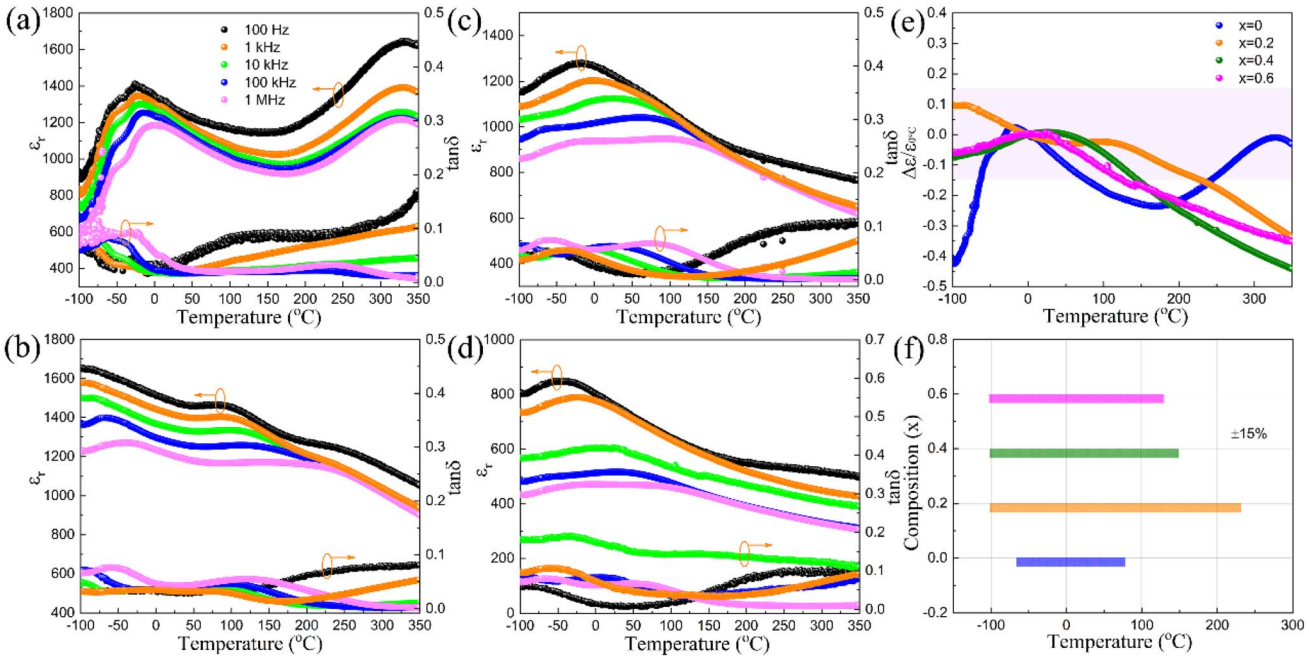

Fig. 6 Temperature dependences of dielectric permittivity ε_r and dielectric loss tanδ for $Sr_{4-x}La_xNa_2Hf_xNb_{10-x}O_{30}$ ceramics: (a) $x = 0$, (b) $x = 0.2$, (c) $x = 0.4$, (d) $x = 0.6$; (e) evolution of $\Delta\varepsilon/\varepsilon_{0°C}$ ($\Delta\varepsilon = \varepsilon_r - \varepsilon_{0°C}$) as a function of temperature for SSNFN ceramic at 10 kHz; (f) temperature range of $\Delta\varepsilon \pm 15\%$.

$= 0$, -100 °C to 227 °C for $x = 0.2$, -100 °C to 145 °C for $x = 0.4$, and -100 °C to 126 °C for $x = 0.6$. Evidently, Hf substitution broadens the temperature-stable range, indicating the potential for temperature-stable dielectric capacitors. The compounds' dielectric loss values remain below 0.1 for x ranging from 0.2 to 0.6, which is also favorable to enhance the energy storage efficiency.

The ferroelectric properties of the compounds were measured through polarization–electric (P–E) curves at room temperature with a triangular waveform at 10 Hz, as depicted in Fig. 7. Saturated hysteresis loops were observed for $x = 0$ and $x = 0.2$, whereas slimmer P–E loops were noted for $x = 0.4$ and 0.6. With the increasing electric field, the maximum polarization P_{max} value rises significantly for compounds, while the remanent polarization P_r values show an apparent increase for $x = 0$ and $x = 0.2$, however, only limited changes were observed for $x = 0.4$ and 0.6. Consequently, larger $\Delta P(P_{max} - P_r)$ values, beneficial for enhancing energy storage efficiency, were obtained for $x = 0.4$ and 0.6. By considering the polarization values of different compounds, it can be found that the maximum polarization value decreases sequentially with rising x: $x = 0 > x = 0.2 > x = 0.4 > x = 0.6$. Similarly, the remanent polarization decreases noticeably: $x = 0 > x = 0.2 > x = 0.6 \approx x = 0.4$, therefore, among the compounds, $x = 0.4$ exhibits the slimmest ferroelectric loop. Normally, dielectric breakdown strength is inversely proportional to the maximum polarization, as such the breakdown strength of $x = 0$, which has the largest polarization is only 90 kV cm^{-1}, then with the Hf substitution, it

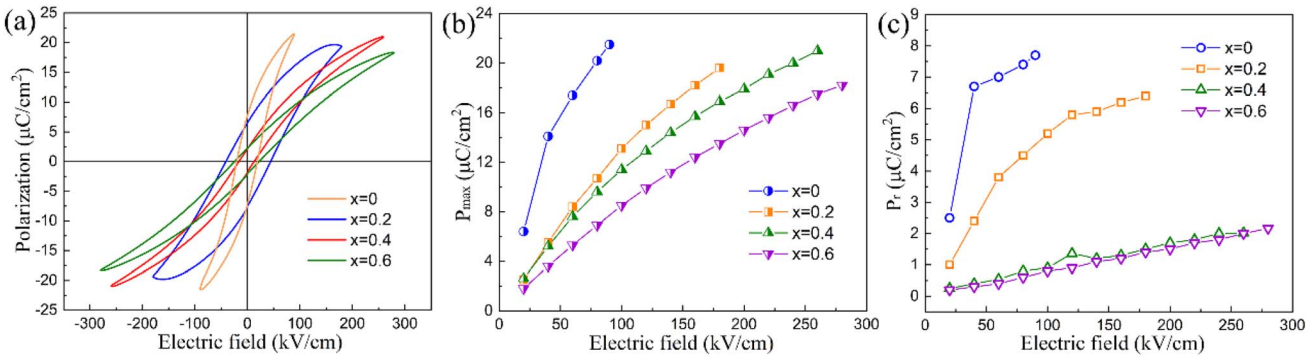

Fig. 7 (a) Polarization–electric field (P–E) curve measured at ambient temperature with a triangular wave form at 10 Hz for $Sr_{4-x}La_xNa_2Hf_xNb_{10-x}O_{30}$ ceramics; (b) the variation in P_{max} with increasing imposed electric field for $Sr_{4-x}La_xNa_2Hf_xNb_{10-x}O_{30}$ ceramics; (c) the variation in P_r with increasing imposed electric field for $Sr_{4-x}La_xNa_2Hf_xNb_{10-x}O_{30}$ ceramics.

gradually increases to 180, 260, and 280 kV cm^{-1} for $x = 0.2$, 0.4, and 0.6 respectively.

To further assess the energy storage capability, unipolar *P–E* loops were evaluated for $x = 0.4$ and $x = 0.6$, which exhibited higher dielectric breakdown strength and lower remanent polarization. As shown in Fig. 8, $x = 0.4$ demonstrates a larger E_b (360 kV cm^{-1}) and a slimmer hysteresis loop. For $x = 0.6$, the E_b is only 240 kV cm^{-1}, with lower energy storage density and efficiency compared to $x = 0.4$. Overall, $x = 0.4$ exhibits the best energy storage properties among the compounds studied. The P_m, P_r, and ΔP values under different electric fields are displayed in Fig. 8(c), it shows gradual increases in P_m and P_r with rising electric field, while ΔP remains relatively stable. The total energy storage density W_{total}, recovery energy storage density W_{rec} and the efficiency η were evaluated and the data are shown in Fig. 8(d). With the increasing imposed electric field, both W_{total} and W_{rec} gradually rise, reaching their maximum values of 3.6 J cm^{-3} and 2.9 J cm^{-3} under the highest electric field endurance of 360 kV cm^{-1}. The energy storage efficiency is approximately 80%, making this compound a promising candidate for energy storage materials. Meanwhile, the improved E_b for $x = 0.4$ is ascribed to many factors such as optimized microstructure, reduced grain size, larger resistance and widened band gap width,[40–43] the E_b value is the result of the interaction of all these factors.

The stability of the energy storage properties at different temperatures and frequencies under the same electric field of 180 kV cm^{-1} is shown in Fig. 9. As the temperature increases from 20 °C to 160 °C, W_{total} remains around 1.35 J cm^{-3}, W_{rec} stays about 1.35 J cm^{-3}, and the efficiency η holds steady at approximately 73%. All these parameters exhibit less than 10% variation, indicating excellent thermal stability of the energy storage performance for the compound. When measuring the *P–E* loops at frequencies ranging from 5 Hz to 100 Hz, W_{total} remains stable while W_{rec} decreases gradually, and η also diminishes with increasing frequency. This suggests that the compound has better thermal stability but relatively strong frequency dispersion, which is consistent with the result of the temperature-dependent dielectric permittivity curves. The energy storage property must consider the energy storage density, efficiency and thermal stability simultaneously, and Table 1 provides the comparative data on the energy storage characteristics of the $x = 0.4$ compound in relation to other tungsten bronze dielectrics.[15,16,20,26,44–46] This research demonstrates a good combination of high energy storage density, energy storage efficiency, and a wide thermally stable range for $x = 0.4$, the density and stable temperature range have surpassed many other systems, revealing the compound's superior comprehensive properties and potential for use in energy storage dielectric capacitors.

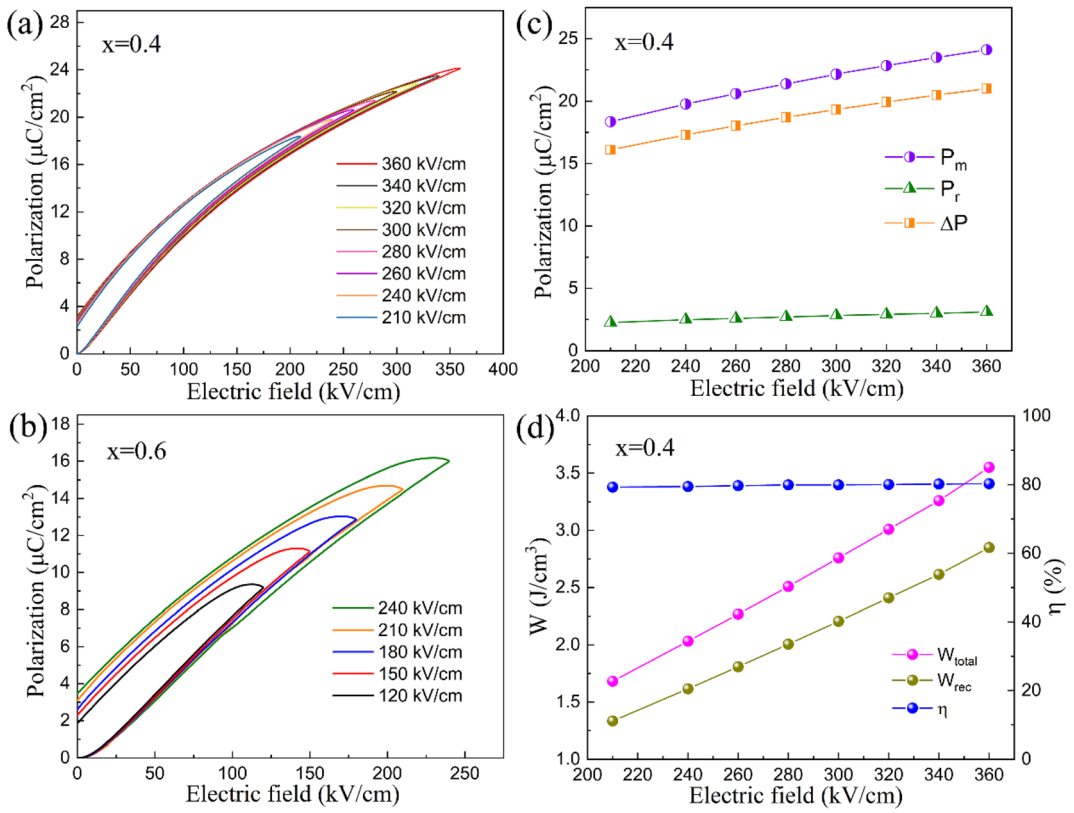

Fig. 8 (a) The variation in unipolar *P–E* loops of $Sr_{4-x}La_xNa_2Hf_xNb_{10-x}O_{30}$ $x = 0.4$ with increasing imposed electric field; (b) the variation in unipolar *P–E* loops of $x = 0.6$ with increasing imposed electric field; (c) the variation in P_{max} and P_r with increasing imposed electric field for $x = 0.4$; (d) the calculated total energy storage density (W_{total}), recoverable energy storage density (W_{rec}) and energy storage efficiency (η) under different electric fields for $x = 0.4$.

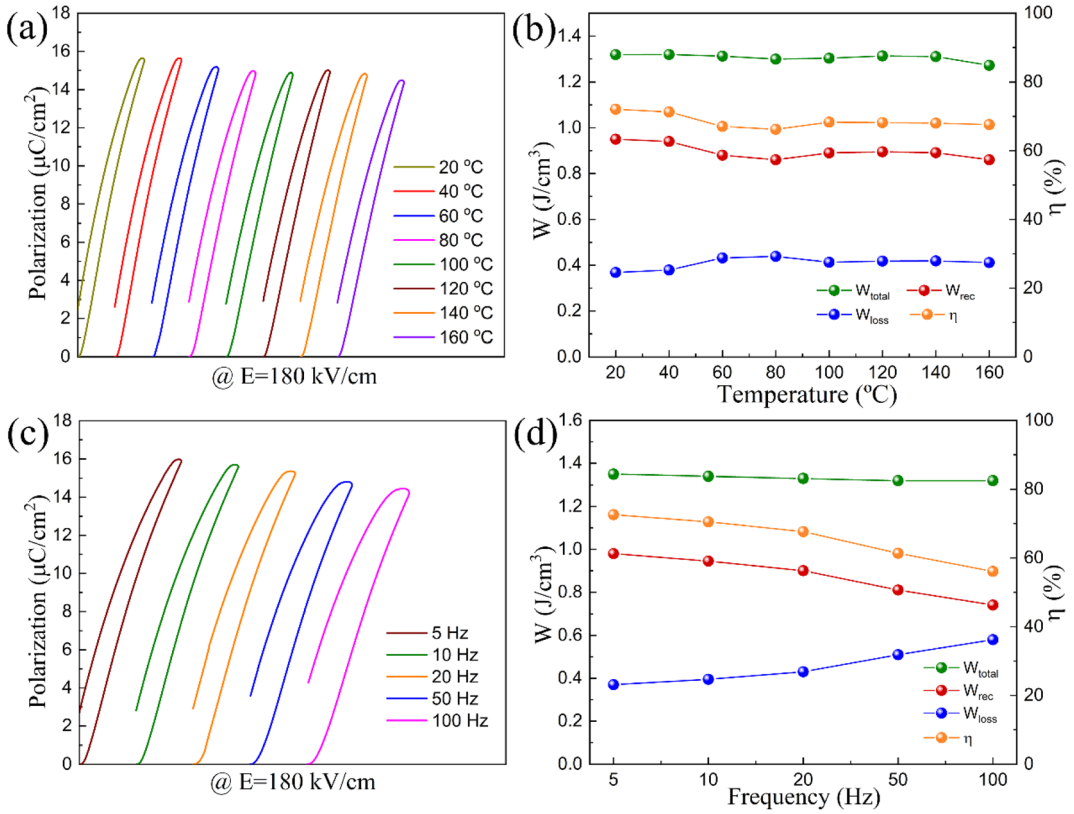

Fig. 9 Stability of the $x = 0.4$ ceramic: (a) the temperature dependence of unipolar P–E loops from 20 to 160 °C under an electric field of 180 kV cm^{-1}; (b) the calculated W_{total}, W_{rec} and η under 180 kV cm^{-1} at different temperatures; (c) the frequency dependence of unipolar P–E loops from 5 Hz to 100 Hz under an electric field of 180 kV cm^{-1}; (d) the calculated W_{total}, W_{rec} and η under 180 kV cm^{-1} at different frequencies.

Table 1 The comparison of the energy storage performance between the current system and other tungsten bronze dielectrics

Composition	W_{rec} (J cm^{-3})	η (%)	Stable temperature range (°C)	Ref.
$Sr_{1.75}Ca_{0.25}NaNb_5O_{15}$	3.23	88.2	25–100	44
$Sr_2Na_{0.8}Ag_{0.2}Nb_5O_{15}$	1.44	82	30–150	16
$Sr_2NaNb_{3.5}Ta_{1.5}O_{15}$	3.99	91.7	20–120	45
$Sr_{1.82}Gd_{0.12}NaNb_5O_{15}$	2.37	94.4	25–100	26
$Sr_3SmNa_2Fe_{0.5}Nb_{9.5}O_{30}$	1.68	80	20–120	20
$Sr_2Na_{0.8}Ag_{0.2}Nb_{4.7}Sb_{0.3}O_{15}$	2.27	93.3	30–130	46
$Sr_{1.88}La_{0.12}NaNb_{4.08}Ta_{0.8}Ti_{0.12}O_{15}$	2.03	94	25–130	15
$Sr_{4-x}La_xNa_2Hf_xNb_{10-x}O_{30}$	2.90	80	20–160	This work

Thermal stability is crucial for assessing the energy-storage capabilities of dielectric capacitors used in harsh environments. This compound provides good thermal stability along with relatively high recoverable energy storage density and efficiency. These are closely related to the Hf cation substitution in the B site for Nb. The cation displacement of Nb and Hf along the polar axis is the origin of ferroelectricity in tungsten bronze structures. However, the differences in cation size, valence, electron distribution and ferroelectric activity between Hf and Nb cations lead to local composition, charge, and lattice disorders within the NbO_6 matrix, inducing the formation of micro-nano polar regions. These are beneficial to reduce the sensitivity of the dielectric constant and ferroelectric polarization to temperature, thus ensuring stable capacitive performance over a wide temperature range. Additionally, a stronger relaxor nature guarantees higher dielectric breakdown strength, greater energy storage density and efficiency. Therefore, with appropriate Hf substitution in the B site, $x = 0.4$ simultaneously achieves a uniform microstructure, larger band gap, higher resistance, stronger relaxor behavior and excellent comprehensive energy storage properties.

4. Conclusions

In summary, $Sr_{4-x}La_xNa_2Hf_xNb_{10-x}O_{30}$ tungsten bronze ceramics were synthesized and characterized. XRD patterns

confirmed the tetragonal tungsten bronze structure for all the compounds. With increasing x, Raman spectroscopy and UV-vis spectrum analyses revealed local structural changes. The most uniform microstructure with the least defects and the highest resistance were observed for $x = 0.4$. Compared to $x = 0$, Hf substitution at the B site significantly enhances the relaxor ferroelectric behavior, and improves the energy storage performance and its thermal stability. Consequently, a high total energy storage density of 3.6 J cm^{-3}, energy storage efficiency of 80%, and good thermal stability are achieved simultaneously for $x = 0.4$ under 360 kV cm^{-1}. This work highlights the significant potential for designing tungsten bronze ceramics for energy storage applications and paves a feasible path for developing new lead-free dielectric capacitors.

Data availability

The original data that support the findings of the present study are available from the corresponding author upon reasonable request.

Author contributions

Wenbin Feng: conceptualization and design of the study, funding acquisition, writing original draft, reviewing, and editing. Lele Ding: performing the experiment, interpretation of data, writing the original draft. Jiajia Zhang: performing the experimental and theoretical analysis. Chunyi Zhu: material preparation, data collection and analysis. Shenzhenyi Song: performing the experiment.

Conflicts of interest

There are no conflicts to declare.

Acknowledgements

This work was supported by National Natural Science Foundation of China under grant number 52102134 and High Level Innovative and Entrepreneurial Personnel Project of Jiangsu Province.

References

1 Z. Ma, Y. Li, Y. Zhao, N. Sun, C. Lu, P. Han, D. Wang, Y. Hu, X. Lou and X. Hao, *J. Mater. Chem. A*, 2023, **11**, 7184–7192.
2 M. Zhang, S. Lan, B. B. Yang, H. Pan, Y. Q. Liu, Q. H. Zhang, J. L. Qi, D. Chen, H. Su, D. Yi, Y. Y. Yang, R. Wei, H. D. Cai, H. J. Han, L. Gu, C.-W. Nan and Y.-H. Lin, *Science*, 2024, **384**, 185–189.
3 L. Yang, X. Kong, F. Li, H. Hao, Z. Cheng, H. Liu, J.-F. Li and S. Zhang, *Prog. Mater. Sci.*, 2019, **102**, 72–108.
4 G. Wang, Z. Lu, Y. Li, L. Li, H. Ji, A. Feteira, D. Zhou, D. Wang, S. Zhang and I. M. Reaney, *Chem. Rev.*, 2021, **121**(10), 6124–6172.
5 P. R. Ren, J. L. Wang, J. J. He, Y. K. Wang, H. Yuan, Y. Hao, T. Frömling, Y. H. Wan, Y. G. Shi and G. Y. Zhao, *Adv. Electron. Mater.*, 2020, **6**, 1901429.
6 F. T. Hu, X. F. Chen, P. Peng, F. Cao, X. L. Dong and G. S. Wang, *J. Am. Ceram. Soc.*, 2018, **101**, 4434–4440.
7 C. Li, J. Liu, W. Bai, S. Wu, P. Zheng, J. Zhang, Z. Pan and J. Zhai, *J. Mater. Chem. A*, 2022, **10**, 9535–9546.
8 H. Zhao, X. Yang, D. Pang and X. Long, *Ceram. Int.*, 2021, **47**, 22734–22740.
9 C. Li, T. Zheng and J. Wu, *Acta Mater.*, 2021, **206**, 116601.
10 H. Pan, F. Li, Y. Liu, Q. Zhang, M. Wang, S. Lan, Y. Zheng, J. Ma, L. Gu, Y. Shen, P. Yu, S. Zhang, L.-Q. Chen, Y.-H. Lin and C.-W. Nan, *Science*, 2019, **365**, 578–582.
11 X. Zhu, M. Fu, M. C. Stennett, P. M. Vilarinho, I. Levin, C. A. Randall, J. Gardner, F. D. Morrison and I. M. Reaney, *Chem. Mater.*, 2015, **27**, 3250–3261.
12 A. Torres-Pardo, R. Jiménez, J. M. González-Calbet and E. García-González, *Inorg. Chem.*, 2011, **50**, 12091–12098.
13 T. Brown, A. P. Brown, D. A. Hall, T. E. Hooper, Y. Li, S. Micklethwaite, Z. Aslam and S. J. Milne, *J. Eur. Ceram. Soc.*, 2021, **41**, 3416–3424.
14 S. D. Xu, S. J. Shen, C. W. Huang, Y. He, X. L. Chao, D. Wu, P. F. Liang, Z. P. Yang, J. B. Lu and L. L. Wei, *ACS Appl. Mater. Interfaces*, 2023, **15**(9), 11642–11651.
15 L. Cao, Y. Yuan, B. Tang, E. Z. Li and S. R. Zhang, *Chem. Eng. J.*, 2021, **421**, 127846.
16 S. Xu, R. Hao, Z. Yan, S. Hou, Z. Peng, D. Wu, P. Liang, X. Chao, L. Wei and Z. Yang, *J. Eur. Ceram. Soc.*, 2022, **42**(6), 2781–2788.
17 W. B. Feng, X. L. Zhu, X. Q. Liu and X. M. Chen, *J. Appl. Phys.*, 2018, **124**, 104102.
18 W. B. Feng, S. D. Long, Y. Wan and D. P. Zhang, *J. Asian Ceram. Soc.*, 2022, **10**, 396–404.
19 C. Luo, X. T. Zheng, P. Zheng, J. Du, Z. A. Niu, K. Zhang, W. F. Bai, Q. L. Fan, L. Zheng and Y. Zhang, *J. Alloys Compd.*, 2023, **933**, 167809.
20 W. Feng, L. Cheng, X. N. Hua, X. Chen, H. Zhang and H. Duan, *RSC Adv.*, 2022, **12**(52), 33816–33824.
21 W. B. Feng, Y. F. Xu, X. G. Li, Y. Y. Wu and J. J. Yang, *J. Mater. Sci: Mater. Electron.*, 2023, **34**, 117.
22 T. Cui, J. Zhang, J. Guo, X. J. Li, S. Guo, Y. Huan, J. Wang and S.-T. Zhang, *J. Mater. Chem. A*, 2022, **10**, 14316–14325.
23 S. W. Li, Z. Yan, Y. F. You, K. Y. Zheng, L. Zhang, X. L. Chao, D. Wu, P. F. Liang, Z. P. Yang, J. B. Lu and L. L. Wei, *Ceram. Int.*, 2024, **50**, 14223–14231.
24 J. J. Lima-Silva, D. Garcia, J. Mendes Filho, J. A. Eiras and A. P. Ayala, *Phys. Status Solidi B*, 2004, **241**, 2001–2006.
25 V. Massarotti, D. Capsoni, M. Bini, C. B. Azzoni, M. C. Mozzati and P. Galinetto, *J. Phys. Chem. C*, 2007, **111**, 6857–6861.
26 L. Cao, Y. Yuan, X. J. Meng, E. Z. Li and B. Tang, *ACS Appl. Mater. Interfaces*, 2022, **14**, 9318–9329.
27 J. J. Gao, J. P. Song, P. Ping and W. Q. Meng, *Ceram. Int.*, 2023, **49**(23), 38432–38438.
28 S. N. H. M. Yunus, K. S. Fhan, B. Johar, N. M. S. Adzali, N. H. Jakfar, C. E. Meng, E. Z. M. Tarmizi and Z. A. Talib, *Mater. Chem. Phys.*, 2023, **309**, 12833.

29 J. Shankar, A. S. Kumar and R. V. S. Kumar, *Ferroelectrics*, 2023, **606**(1), 207–218.
30 H. R. Ye, F. Yang, Z. B. Pan, D. Hu, X. J. Lv, H. X. Chen, F. F. Wang, J. S. Wang, P. Li, J. W. Chen, J. J. Liu and J. W. Zhai, *Acta Mater.*, 2021, **203**, 116484.
31 Zulhadjri, T. P. Wendari, R. Ramadhani, Y. E. Putri and Imelda, *Ceram. Int.*, 2021, **47**(16), 23549–23557.
32 J. D. Bobić, R. M. Katiliute, M. Ivanov, M. M. Vijatović Petrović, N. I. Ilić, A. S. Džunuzović, J. Banys and B. D. Stojanović, *J. Mater. Sci.: Mater. Electron.*, 2016, **27**, 2448–2454.
33 S. Samanta, V. Sankaranarayanan and K. Sethupathi, *Ferroelectrics*, 2019, **202**(1), 153–162.
34 X. Xiong, H. Liu, J. Zhang, L. L. da Silva, Z. H. Sheng, Y. H. Yao, G. Wang, M. Hinterstein, S. J. Zhang and J. Chen, *Adv. Mater.*, 2024, 2410088.
35 C. B. Long, Z. Q. Su, A. W. Xu, H. Huang, L. J. Liu, L. Gu, W. Ren, H. J. Wu and X. D. Ding, *Nano Energy*, 2024, **124**, 109493.
36 G. Wang, J. Li, X. Zhang, Z. Fan, F. Yang, A. Feteira, D. Zhou, D. C. Sinclair, T. Ma, X. Tan, D. Wang and I. M. Reaney, *Energy Environ. Sci.*, 2019, **12**, 582–588.
37 H. Liu, Z. Sun, J. Zhang, H. J. Luo, Q. H. Zhang, Y. H. Yao, S. Q. Deng, H. Qi, J. Liu, L. C. Gallington, J. C. Neuefeind and J. Chen, *J. Am. Chem. Soc.*, 2023, **145**(21), 11764–11772.
38 E. García-González, A. Torres-Pardo, R. Jiménez and J. M. González-Calbet, *Chem. Mater.*, 2007, **19**, 3575–3580.
39 L. L. Wei, Z. P. Yang, R. Gu and H. M. Ren, *J. Am. Ceram. Soc.*, 2010, **93**, 1978–1983.
40 E. Kröll, A. Dubey, V. V. Shvartsman and D. C. Lupascu, *J. Eur. Ceram. Soc.*, 2023, **43**(15), 6864–6874.
41 P. Zheng, X. T. Zheng, J. Q. Wang, L. S. Sheng, L. Zheng, Q. L. Fan, W. F. Bai and Y. Zhang, *Appl. Mater. Today*, 2024, **39**, 102326.
42 C. Wu, X. M. Qiu, W. W. Ge, L. Y. Chen, C. Y. Liu, H. W. Zhao and L. Li, *J. Alloys Compd.*, 2023, **948**, 169723.
43 G. W. Yan, J. Sun, B. J. Fang, S. Zhang, X. L. Lu and J. N. Ding, *J. Am. Ceram. Soc.*, 2024, **107**, 5598–5607.
44 X. Z. Zhang, W. B. Ye, X. Y. Bu, P. Zheng, L. L. Li, F. Wen, W. F. Bai, L. Zheng and Y. Zhang, *Dalton Trans.*, 2021, **50**, 124–130.
45 X. Z. Zhang, H. L. Wang, X. Y. Bu, P. Zheng, L. L. Li, F. Wen, W. F. Bai, J. J. Zhang, L. Zheng, J. W. Zhai and Y. Zhang, *Inorg. Chem.*, 2021, **60**(9), 6559–6568.
46 S. Xu, S. Shen, R. Hao, Z. Peng, F. Zhang, D. Wu, P. Liang, X. Chao, L. Wei and Z. Yang, *Chem. Eng. J.*, 2022, **433**, 133812.